Supporting Information for "Planetary boundary layer height modulates aerosol – water vapour interactions during winter in the megacity of Delhi"

Subha S. Raj[1,2], Ovid O. Krüger[3], Amit Sharma[1,a], Upasana Panda[1,4], Christopher Pöhlker[3], David Walter[3], Jan-David Förster[3], Rishi Pal Singh[5], Swetha S.[1,b], Thomas Klimach[3], Eoghan Darbyshire[6,c], Scot T. Martin[7,8], Gordon McFiggans[6], Hugh Coe[6], James Allan[6,9], Ravikrishna R.[10,2], Vijay Kumar Soni[5], Hang Su[3], Meinrat O. Andreae[3,11,12], Ulrich Pöschl[3], Mira L. Pöhlker[3]and Sachin S. Gunthe[1,2]

[1]EWRE Division, Department of Civil Engineering, Indian Institute of Technology Madras, Chennai, India

[2]Laboratory for Atmospheric and Climate Sciences, Indian Institute of Technology Madras, Chennai, India

[3]Multiphase Chemistry and Biogeochemistry Departments, Max Planck Institute for Chemistry, Mainz, Germany

[4]Department of Environment and Sustainability, CSIR Institute of Minerals and Materials Technology, Bhubaneswar, India

[5]India Meteorological Department, New Delhi, India

[6]Department of Earth and Environmental Sciences, School of Natural Sciences, University of Manchester, Manchester, UK

[7]John A. Paulson School of Engineering and Applied Sciences, Harvard University, Cambridge, MA, USA

[8]Department of Earth and Planetary Sciences, Harvard University, Cambridge, MA, USA

[9]National Centre for Atmospheric Science, University of Manchester, Manchester, UK

[10]Department of Chemical Engineering, Indian Institute of Technology Madras, Chennai, India

[11]Scripps Institution of Oceanography, University of California San Diego, La Jolla, CA, USA

[12]Department of Geology and Geophysics, King Saud University, Riyadh, Saudi Arabia

[a]now at: Department of Civil and Infrastructure Engineering, Indian Institute of Technology Jodhpur, Karwar, Jodhpur, India

[b]now at: CSIR Fourth Paradigm Institute, Bengaluru, India

August 9, 2021, 8:56am

[c]now at: The Conflict and Environment Observatory, Hebden Bridge, West Yorkshire, UK

Corresponding author: Subha S. Raj (subhasraj89@gmail.com), Mira L. Pöhlker(m.pohlker@mpic.de), Sachin S. Gunthe (s.gunthe@iitm.ac.in)

Contents of this file

1. Text S1 to S2
2. Figures S1 to S12
3. Tables S1 to S5

Additional Supporting Information (Files uploaded separately)

1. Caption for Dataset S1

Introduction

The data set provided in .csv format contains the PBL height using various model simulations used in this study.

Supporting explanations, measurement data, and analysis results discussed in the manuscript are provided in the following figures and tables.

Text S1. We observed multiple periods with low solar radiation as shown in panel (b) of Figure S5. These periods could have faster nocturnal radiative cooling of the atmosphere and result in an increase in the inversion layer depth (Stull, 2012). These were classified as the weak inversion periods. During rest of the campaign, the strong solar radiation would have slowed down the nocturnal cooling of the atmosphere. Also the high RH near surface observed during these periods could have caused more heat transfer to the atmosphere above the ground (Pasricha et al., 2003; Still et al., 1998). This results in the surface air being cooler than the air above it and cause lowering of the planetary boundary layer height (H_{BL}). These periods were classified as the strong inversion periods. The above observation and hypothesis fits well with the PBL simulations by WRF model, which showed higher H_{BL} during nighttime of weak inversion periods and lower H_{BL} during nighttime of strong inversion periods. The daytime H_{BL} remained high for both the periods.

Text S2 The 3-day air mass back trajectories (BT) in the top panel of Figure S6 and the bottom panel of Figure S7 shows longer trajectories compared to that showed in the bottom panel of Figure S9, because a constant height of 1000 m was selected in the former as the top of the HYSPLIT model (Stein et al., 2015). The same analysis was done using the WRF modelled H_{BL} as the top of the model, which resulted in similar but shorter BTs as shown in Figure S9.

Data Set S1. Time series data of model simulations of planetary boundary layer height (H_{BL}; m) using the WRF and the HYSPLIT model from 05 Feb to 02 Mar 2018. The first column contains the date and time in Indian Standard time (UTC + 05:30) of each entry of H_{BL} simulations in the remaining columns. The second and third column contains the

simulations of WRF using the Bulk-Richardson number method and the TKE method respectively. The fourth column contains the mixing depth values from HYSPLIT model.

References

Pasricha, P. K., Gera, B. S., Shastri, S., Maini, H. K., John, T., Ghosh, A. B., ... Garg, S. C. (2003). Role of the water vapour greenhouse effect in the forecasting of fog occurrence. *Boundary-Layer Meteorology*, *107*(2), 469–482. doi: 10.1023/A:1022128800130

Stein, A. F., Draxler, R. R., Rolph, G. D., Stunder, B. J. B., Cohen, M. D., & Ngan, F. (2015). NOAA's HYSPLIT atmospheric transport and dispersion modelling system. *Bulletin of the American Meteorological Society*, *96*(12), 2059–2077. doi: 10.1175/BAMS-D-14-00110.1

Still, M., Venzke, H., Durst, F., & Melling, A. (1998). Influence of humidity on the convective heat transfer from small cylinders. *Experiments in Fluids*, *24*(2), 141–150. doi: 10.1007/s003480050161

Stull, R. B. (2012). *An introduction to boundary layer meteorology* (Vol. 13). Springer Science & Business Media.

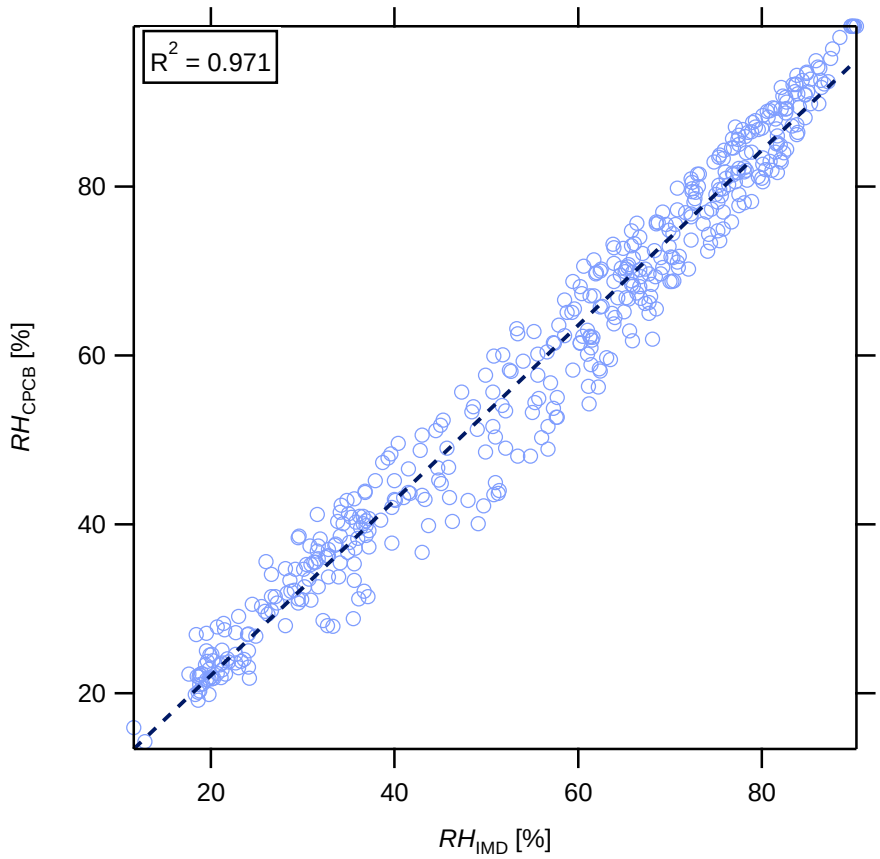

Figure S1. Correlation between concomitant relative humidity measurements in India Meteorological Department (IMD) or the campaign site and the Central Pollution Control Board site (CPCB).

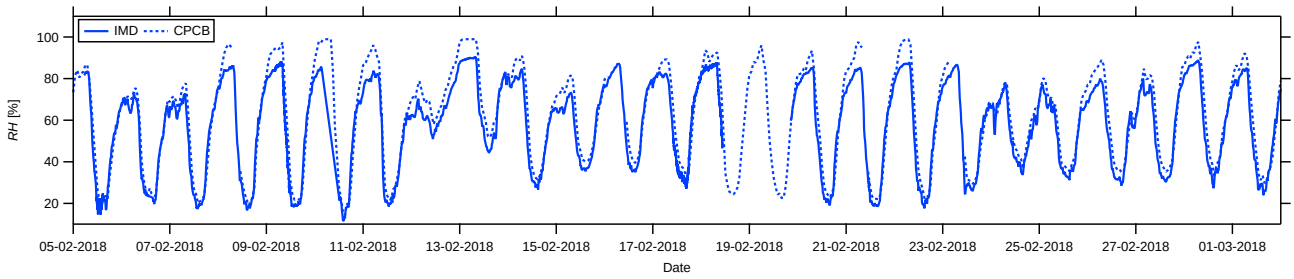

Figure S2. Temporal evolution of concomitant relative humidity measurements in India Meteorological Department (IMD) or the campaign site and the Central Pollution Control Board site (CPCB).

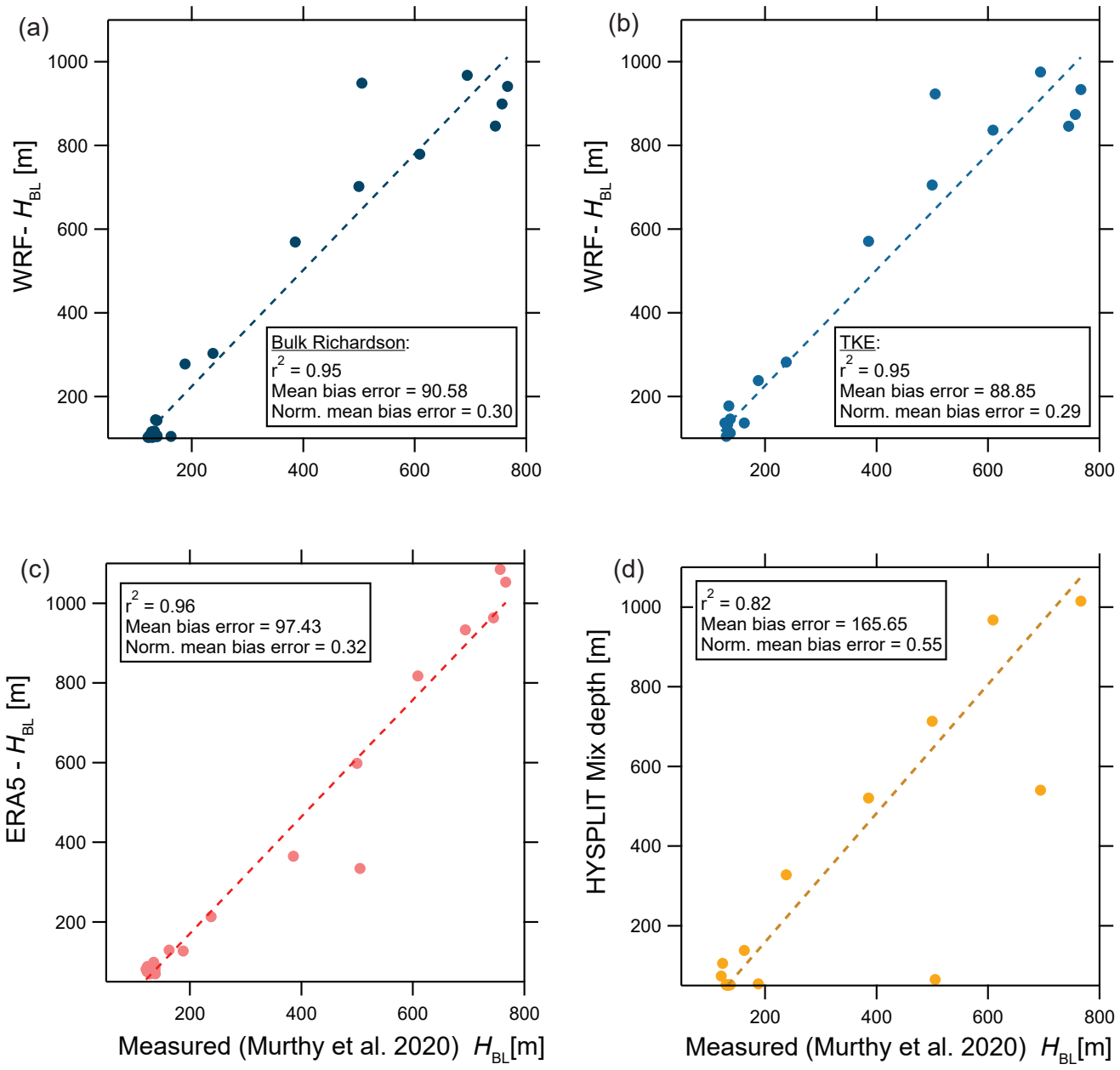

Figure S3. Comparison of modelled planetary boundary layer height from (a): WRF model using Bulk Richardson number, (b) in WRF model using turbulence kinetic energy (TKE), (c) ECMWF satellite reanalysis data (ERA5) and (d) HYSPLIT model with measured data is shown as correlation plots.

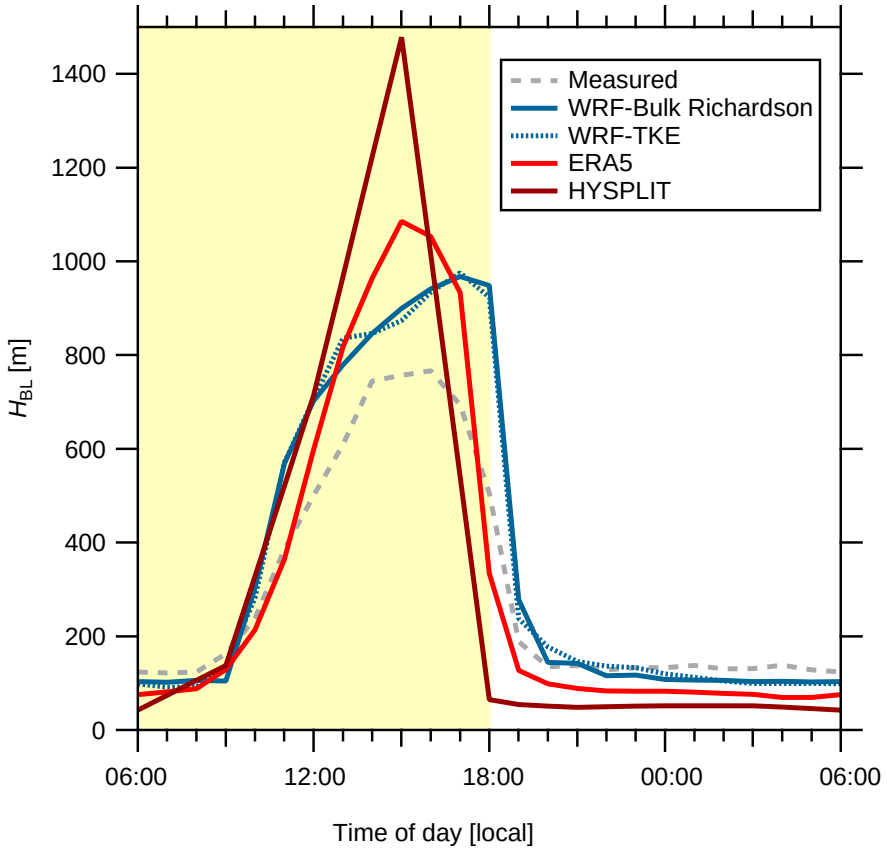

Figure S4. The campaign-average diurnal variation of planetary boundary layer height (H_{BL}): modeled by the WRF model using Bulk Richardson number method (blue solid line) and TKE method (blue dotted line); ECMWF satellite reanalysis ERA5 data (light red solid line); HYSPLIT model (dark red solid line); measured by ceilometer (grey dashed line).

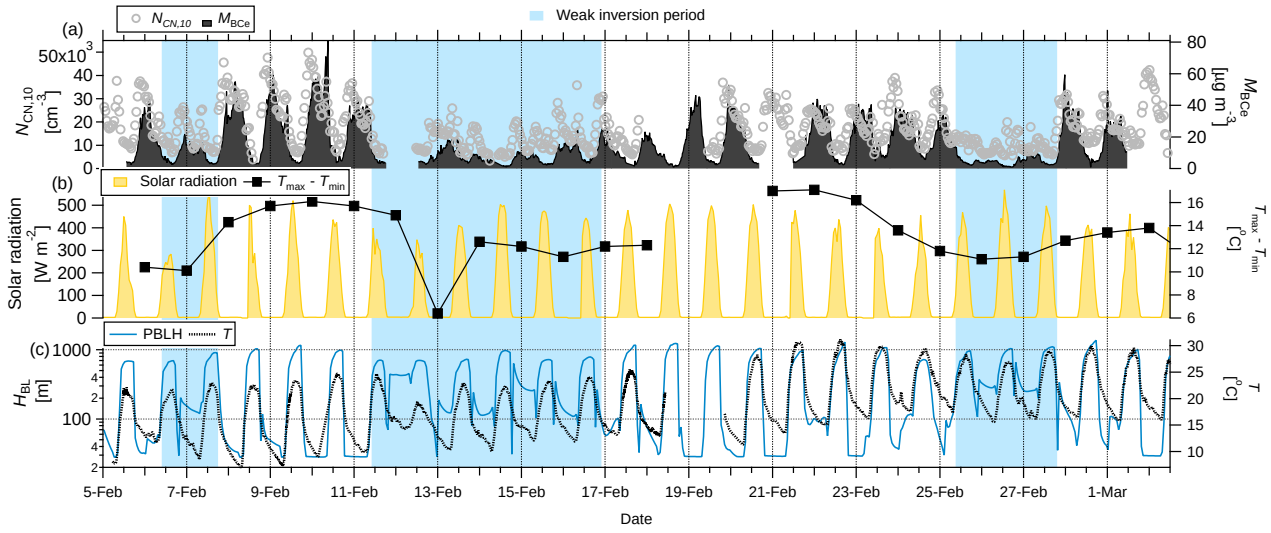

Figure S5. Temporal evolution of the (a): Total particle number concentration in the size range ∼10 to 370 nm ($N_{\mathrm{CN},10}$, cm^{-3}) on the left axis and mass concentration of equivalent BC ($M_{\mathrm{BC,e}}$, μg m^{-3}) on the right axis; (b): Solar radiation (W m^{-2}) on the left axis and difference between maximum and minimum temperature in the period, 12:00:00 LT to 11:59:59 LT (T_{max} - T_{min}, °C) of each diurnal cycle; (c): Planetary boundary layer height (H_{BL}) modelled in WRF using Bulk Richardson number method on the left axis and temperature (T, °C)on the right axis.

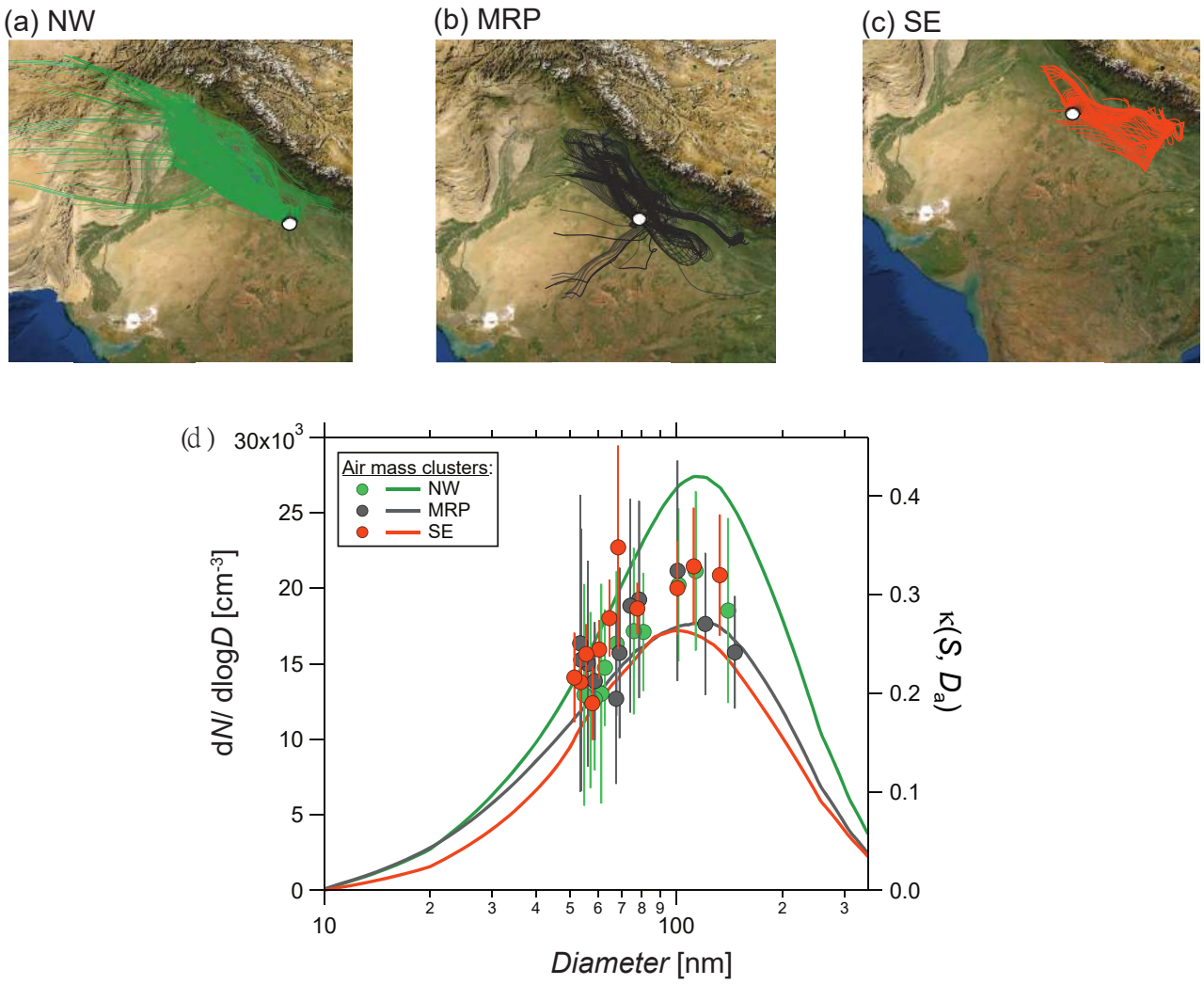

Figure S6. The 3-day back trajectory during (a): NW air mass, (b): MRP air mass and (c): SE air mass is shown. The white dot denotes the location of campaign site in Delhi. The average aerosol number size distribution (left axis) and hygroscopicity distribution (right axis) during each air mass is shown in (c).

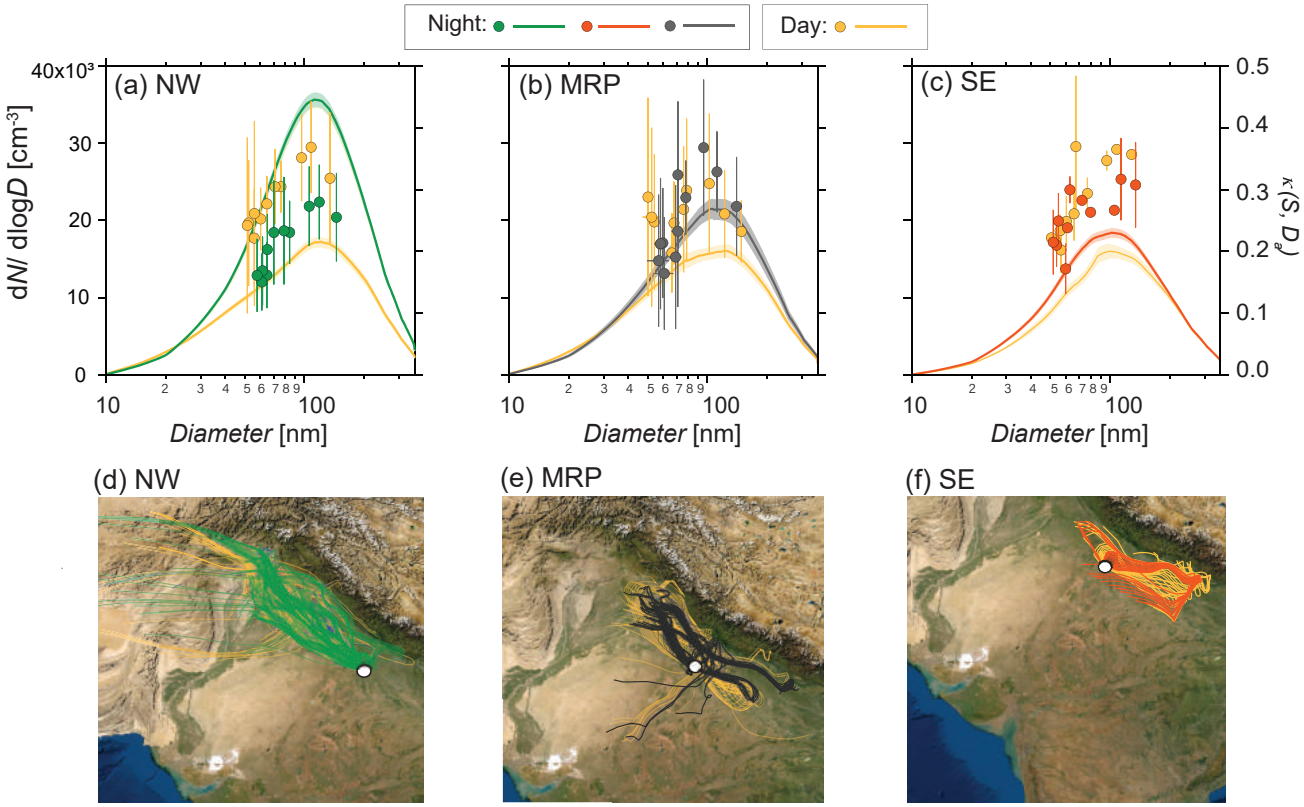

Figure S7. The average aerosol number size distribution (left axis) and hygroscopicity distribution (right axis) during (a): NW air mass, (b): MRP air mass and (c): SE air mass resolved into daytime (yellow) and nighttime (colour of respective air mass) are shown.The 3-day back trajectory resolved into daytime (yellow) and nighttime (colour of respective air mass) during (a): NW air mass, (b): MRP air mass and (c): SE air mass is shown. The white dot denotes the location of campaign site in Delhi.

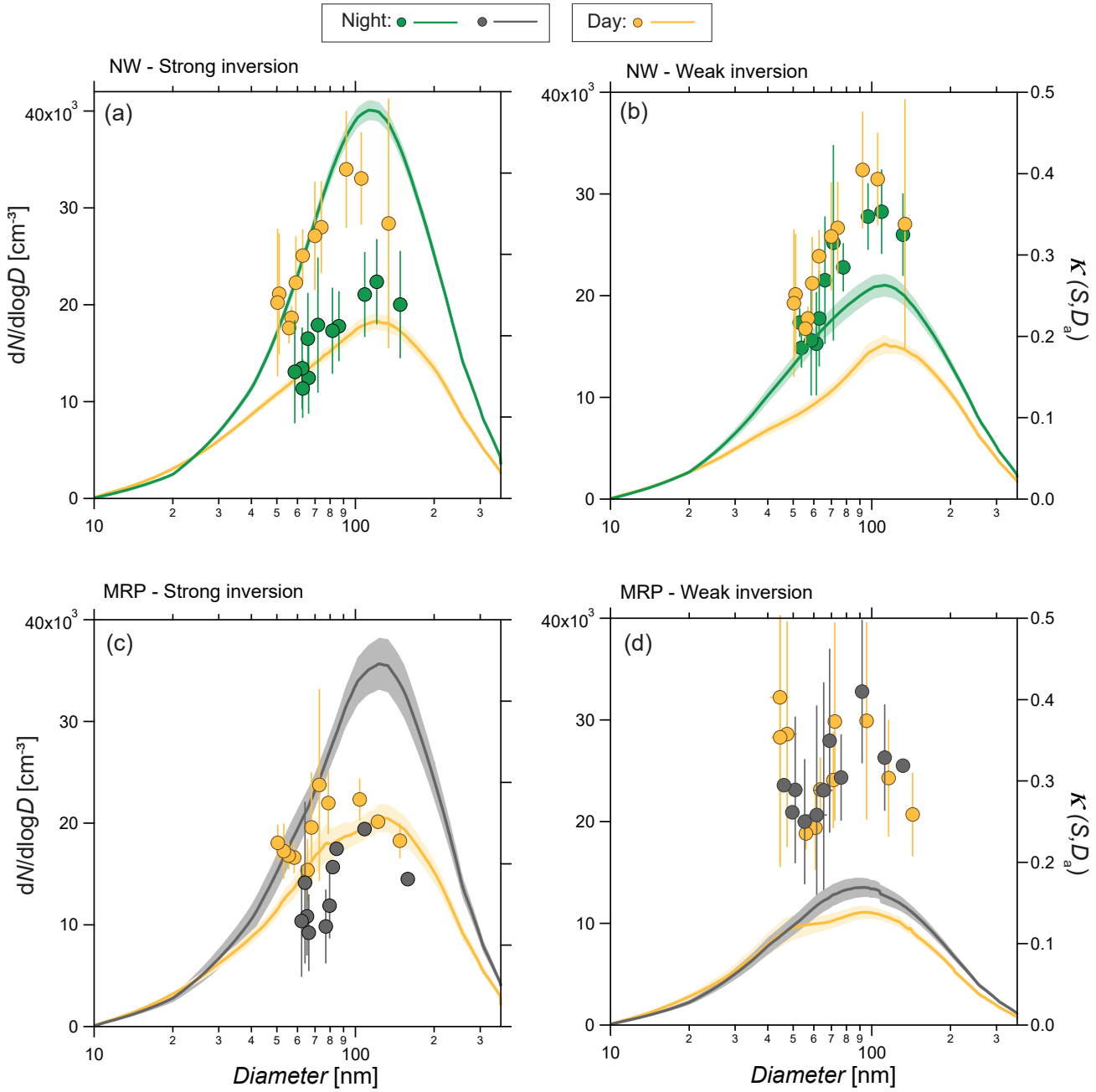

Figure S8. Average aerosol number size distribution (left axis) and hygroscopicity distribution (right axis) during daytime and nighttime for (a): NW under strong inversion periods; (b): NW under weak inversion periods; (c): MRP under strong inversion periods and (d): MRP under weak inversion periods.

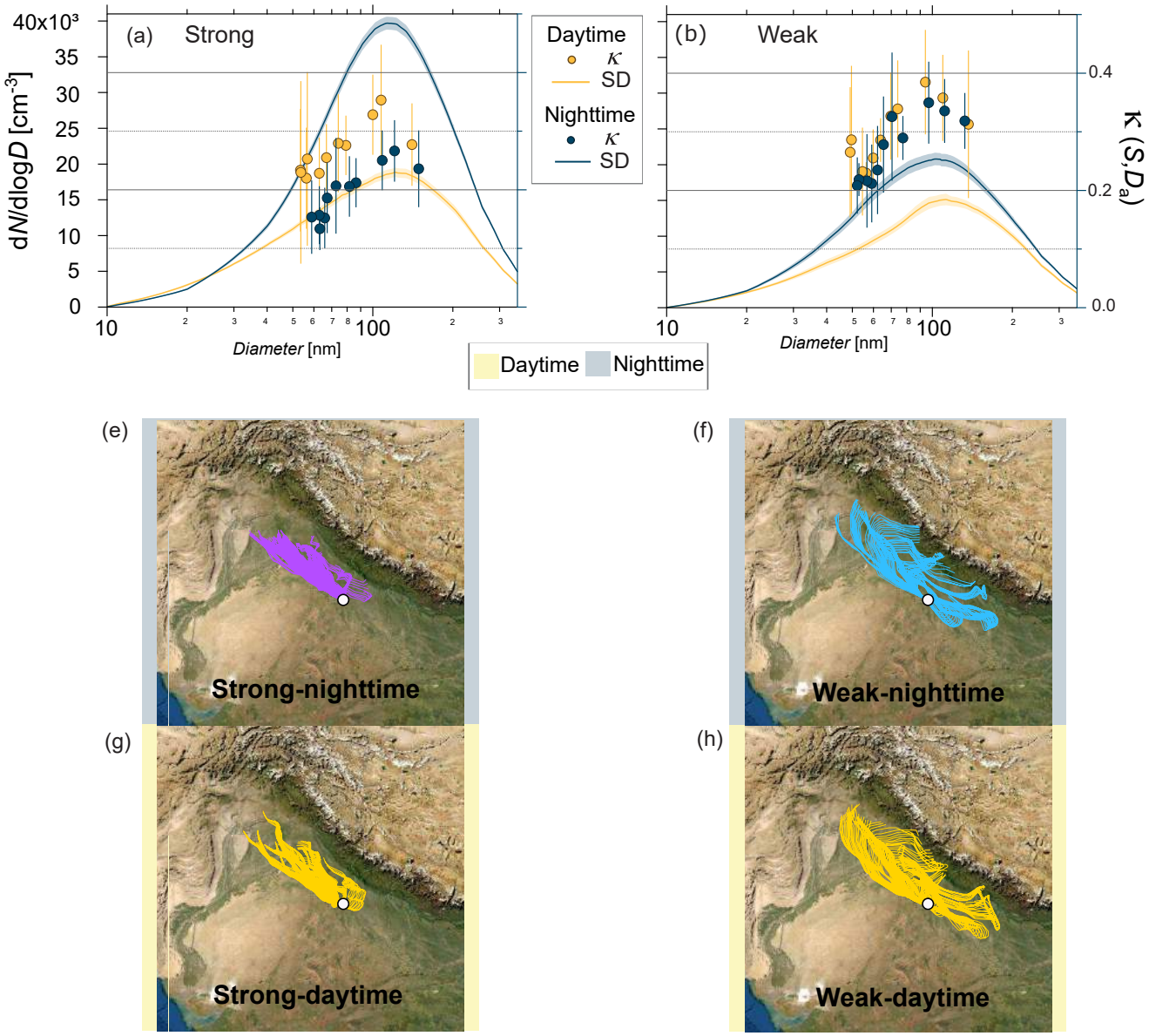

Figure S9. Average aerosol number size distribution (left axis) and hygroscopicity distribution (right axis) during daytime and nighttime for (a): Strong inversion periods and (b): Weak inversion periods. The 3-day back trajectories retrieved using the WRF modelled H_{BL} as the top of model are shown during, (e) strong inversion-nighttime (f) weak inversion-nighttime, (g) strong inversion-daytime and (h) weak inversion-daytime. The white dot denotes the location of campaign site in Delhi.

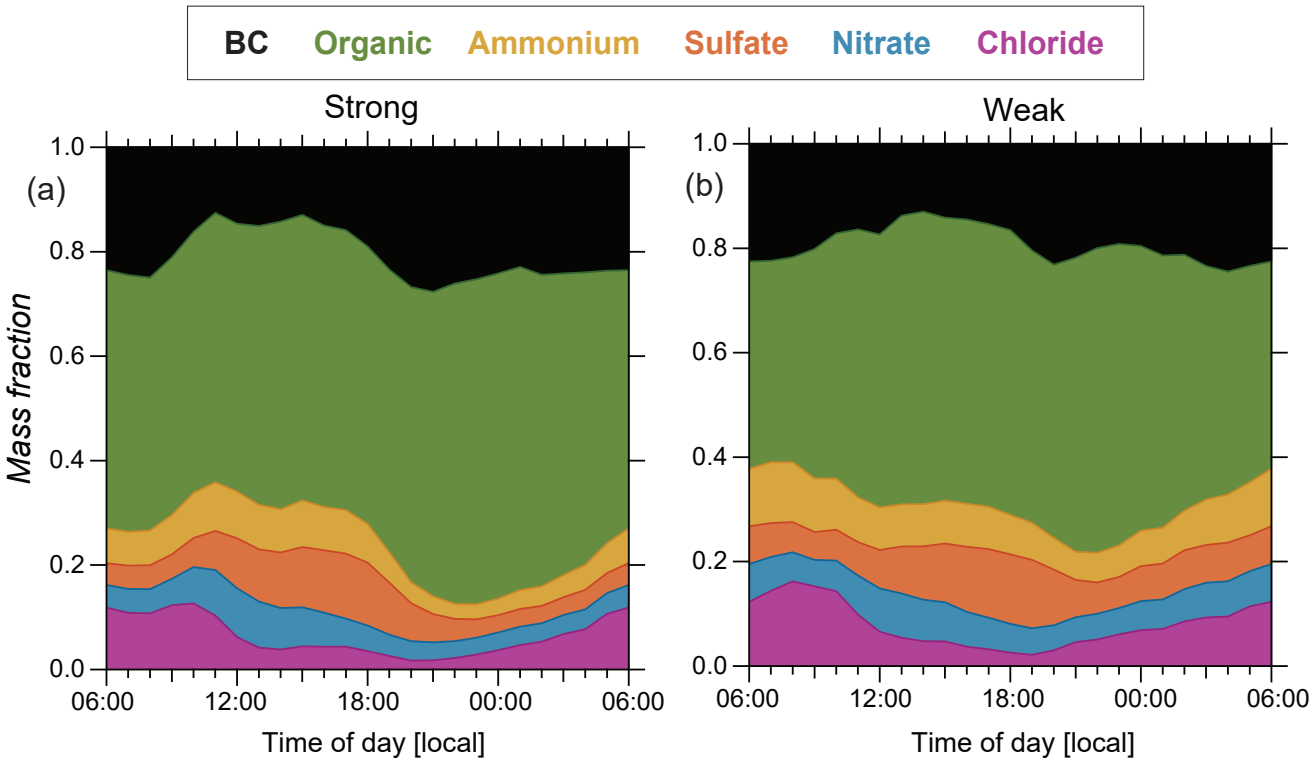

Figure S10. Average diurnal variation of NR-PM1 components such as BC, organics, ammonium, sulfate, nitrate and chloride during (a): strong inversion periods and (b): weak inversion periods.

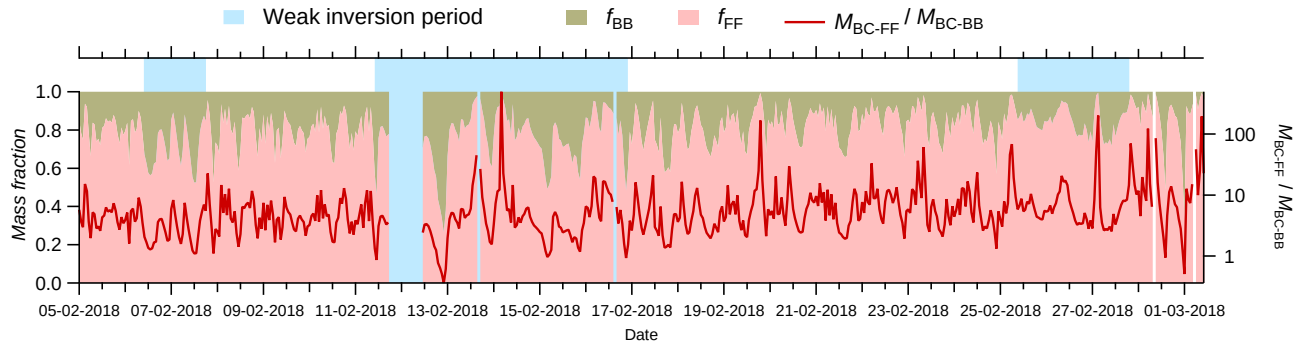

Figure S11. Temporal evolution of the mass fractions of equivalent black carbon (BC) associated with biomass burning (f_{BB}) and fossil fuel combustion (f_{FF}) on the left axis; ratio of mass of equivalent BC associated with fossil fuel combustion to that associated with biomass burning ($M_{\mathrm{BC\text{-}FF}}$ / $M_{\mathrm{BC\text{-}BB}}$)

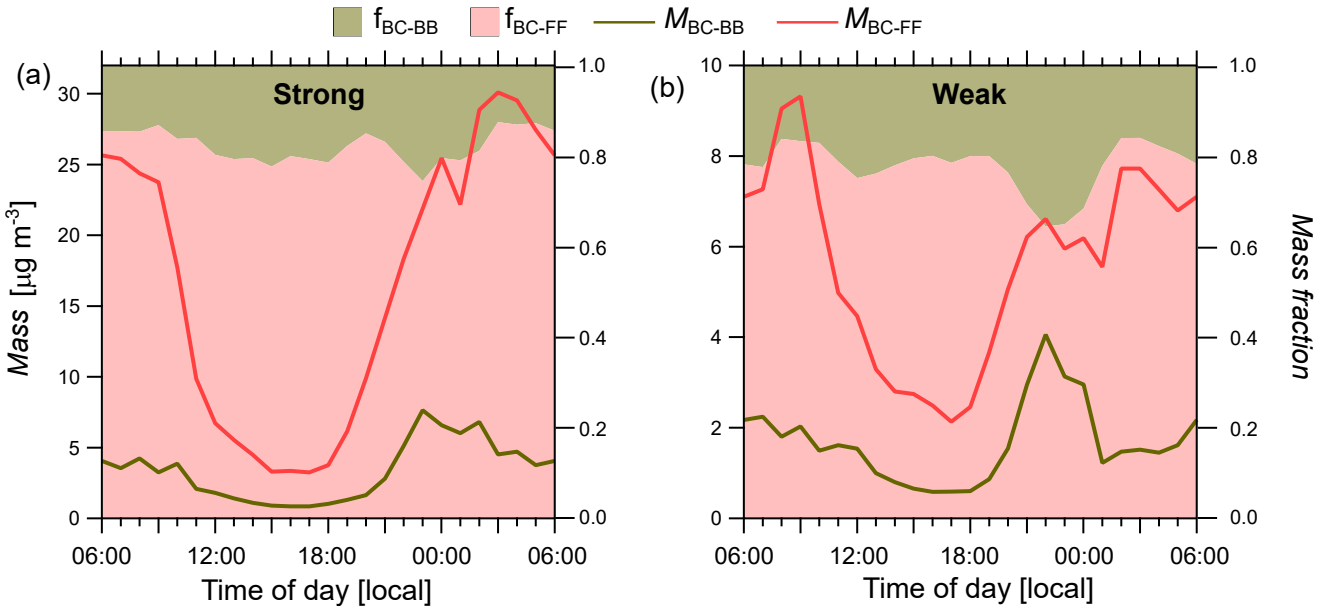

Figure S12. Average diurnal variation of mass of equivalent black carbon associated with biomass burning ($M_{\mathrm{BC\text{-}BB}}$) and fossil fuel combustion ($M_{\mathrm{BC\text{-}FF}}$) on the left axis; and fraction of equivalent black carbon associated with biomass burning ($f_{\mathrm{BC\text{-}BB}}$) and fossil fuel combustion ($f_{\mathrm{BC\text{-}FF}}$) on the right axis for (a): strong inversion and (b): weak inversion periods.

Table S1. Comparison of modelled planetary boundary layer height using different methods with measured data is tabulated.

	WRF-Bulk Richardson	WRF-TKE	ERA5	HYSPLIT
Mean bias error	90.58	88.85	97.43	165.65
Normalized mean bias error	0.30	0.29	0.32	0.55

Table S2. The time of occurrence of strong and weak inversion periods during the campaign is tabulated. All dates indicate year 2018 and all times are in local time (UTC + 05:30).

Period	Time of occurrence
Strong inversion	05 Feb 00:30 to 06 Feb 09:30
	07 Feb 19:30 to 11 Feb 09:30
	16 Feb 22:30 to 25 Feb 08:30
	27 Feb 20:30 to 02 Mar 23:30
Weak inversion	06 Feb 10:30 to 07 Feb 18:30
	11 Feb 10:30 to 16 Feb 21:30
	25 Feb 09:30 to 27 Feb 19:30

Table S3. Probability (%) of occurrence of strong inversion nighttime, weak inversion nighttime and daytime in each H_{BL} bin. H_{BL} bins are defines as minimum to 1st quartile, 1st to 2nd quartile, 2nd to 3rd quartile and 3rd quartile to maximum.

H_{BL}:	28 to 50 m	50 to 158 m	158 to 685 m	685 to 1374 m
Strong-nighttime	60 %	34 %	5 %	1 %
Weak-nighttime	5 %	39 %	56 %	0 %
Daytime	9 %	13 %	28 %	49 %

Table S4. CCN properties measured during strong inversion periods resolved into daytime and nighttime in Delhi shown as a function of effective supersaturation achieved inside the CCNC. The S levels are average values measure with a standard deviation of ∼0.001 %. All other values are expressed as average ± standard deviation. Parameters tabulated are: midpoint activation diameter ($D_{\mathrm{a}}(S)$), hygroscopicity from size-resolved CCN measurements ($\kappa(S,\ D_a)$), width of the CCN activation curve ($\sigma(S)$), maximum activated fraction ($MAF(S)$), total CCN concentration ($N_{\mathrm{CCN}}(S)$), total particle concentration in the size range ∼10 to 370 nm ($N_{\mathrm{CN,10}}$), CCN efficiency ($N_{\mathrm{CCN}}(S)/N_{\mathrm{CN,10}}$), and number of samples for each S levels (n).

S [%]	$D_{\mathrm{a}}(S)$ [nm]	$\kappa(S,\ D_a)$	$\sigma(S)$ [nm]	$MAF(S)$	$N_{\mathrm{CCN}}(S)$ [cm^{-3}]	$N_{\mathrm{CN,10}}$ [cm^{-3}]	$N_{\mathrm{CCN}}(S)$ $/N_{\mathrm{CN,10}}$	n
Strong inversion-daytime:								
0.14	140 ± 12	0.28 ± 0.07	24 ± 7	0.91 ± 0.13	3527 ± 1793	13622 ± 5059	0.26 ± 0.10	18
0.17	110 ± 11	0.35 ± 0.09	20 ± 8	0.90 ± 0.14	4742 ± 2225	12799 ± 4240	0.36 ± 0.13	23
0.21	98 ± 9	0.33 ± 0.07	24 ± 10	0.96 ± 0.09	6845 ± 2995	14553 ± 5513	0.47 ± 0.13	22
0.32	79 ± 7	0.28 ± 0.05	21 ± 8	0.95 ± 0.08	7661 ± 3958	14194 ± 7328	0.54 ± 0.10	20
0.36	74 ± 8	0.28 ± 0.08	19 ± 10	0.94 ± 0.10	8760 ± 5323	15249 ± 7972	0.57 ± 0.12	19
0.43	67 ± 5	0.25 ± 0.06	20 ± 6	0.98 ± 0.08	10275 ± 5707	15256 ± 6921	0.66 ± 0.13	20
0.50	63 ± 7	0.23 ± 0.06	18 ± 6	0.95 ± 0.11	10813 ± 6696	15625 ± 7404	0.66 ± 0.13	20
0.58	57 ± 7	0.25 ± 0.15	15 ± 4	0.99 ± 0.08	12607 ± 8411	16570 ± 9996	0.74 ± 0.10	19
0.61	56 ± 6	0.22 ± 0.09	16 ± 6	0.98 ± 0.08	11553 ± 6744	15729 ± 7709	0.72 ± 0.13	21
0.65	53 ± 7	0.23 ± 0.10	15 ± 10	0.99 ± 0.06	12212 ± 6347	16123 ± 6836	0.74 ± 0.12	18
0.69	54 ± 10	0.23 ± 0.16	14 ± 7	0.99 ± 0.08	9647 ± 4036	13506 ± 4003	0.70 ± 0.12	19
Strong inversion-nighttime								
0.14	149 ± 15	0.24 ± 0.07	33 ± 9	0.69 ± 0.15	6155 ± 3062	28042 ± 7231	0.22 ± 0.11	22
0.17	121 ± 7	0.27 ± 0.05	30 ± 5	0.72 ± 0.15	8570 ± 3986	26092 ± 7074	0.33 ± 0.14	22
0.21	109 ± 8	0.25 ± 0.05	33 ± 6	0.75 ± 0.15	10271 ± 4609	26265 ± 7610	0.39 ± 0.14	21
0.32	86 ± 6	0.21 ± 0.04	28 ± 5	0.79 ± 0.13	13748 ± 5542	26171 ± 8206	0.53 ± 0.15	21
0.36	82 ± 7	0.21 ± 0.05	27 ± 8	0.82 ± 0.12	14934 ± 5893	26233 ± 8750	0.57 ± 0.13	22
0.43	73 ± 8	0.21 ± 0.08	25 ± 7	0.79 ± 0.13	14542 ± 7099	25605 ± 9825	0.57 ± 0.14	20
0.50	67 ± 7	0.19 ± 0.06	22 ± 12	0.81 ± 0.13	15615 ± 7545	25338 ± 9344	0.61 ± 0.14	21
0.58	66 ± 7	0.15 ± 0.05	24 ± 9	0.80 ± 0.12	15404 ± 8335	24635 ± 9083	0.60 ± 0.15	23
0.61	63 ± 9	0.16 ± 0.05	23 ± 10	0.82 ± 0.12	17373 ± 7533	27042 ± 7815	0.63 ± 0.16	22
0.65	63 ± 7	0.13 ± 0.04	22 ± 7	0.82 ± 0.12	17049 ± 6846	26964 ± 7762	0.63 ± 0.15	24
0.69	59 ± 7	0.15 ± 0.06	20 ± 8	0.87 ± 0.12	18289 ± 7678	26237 ± 8178	0.69 ± 0.15	25

Table S5. CCN properties measured during weak inversion periods resolved into daytime and nighttime in Delhi shown as a function of effective supersaturation achieved inside the CCNC. The S levels are average values measure with a standard deviation of ∼0.001 %. All other values are expressed as average ± standard deviation. Parameters tabulated are: midpoint activation diameter ($D_a(S)$), hygroscopicity from size-resolved CCN measurements ($\kappa(S,\ D_a)$), width of the CCN activation curve ($\sigma(S)$), maximum activated fraction ($MAF(S)$), total CCN concentration ($N_{CCN}(S)$), total particle concentration in the size range ∼10 to 370 nm ($N_{CN,10}$), CCN efficiency ($N_{CCN}(S)/N_{CN,10}$), and number of samples for each S levels (n).

S [%]	$D_a(S)$ [nm]	$\kappa(S,\ D_a)$	$\sigma(S)$ [nm]	$MAF(S)$	$N_{CCN}(S)$ [cm^{-3}]	$N_{CN,10}$ [cm^{-3}]	$N_{CCN}(S)$ /$N_{CN,10}$	n
Weak inversion-daytime:								
0.14	137 ± 14	0.31 ± 0.13	22 ± 6	0.98 ± 0.05	3079 ± 1972	10546 ± 4584	0.28 ± 0.09	15
0.17	109 ± 8	0.36 ± 0.07	18 ± 5	0.99 ± 0.06	4279 ± 2158	9722 ± 3058	0.42 ± 0.12	16
0.21	94 ± 7	0.38 ± 0.09	15 ± 5	0.98 ± 0.08	4614 ± 1793	9131 ± 2625	0.50 ± 0.11	15
0.32	74 ± 5	0.34 ± 0.08	14 ± 5	0.98 ± 0.07	6469 ± 2299	10298 ± 3678	0.63 ± 0.07	14
0.36	70 ± 5	0.33 ± 0.07	14 ± 8	0.99 ± 0.10	6981 ± 3475	10525 ± 5166	0.67 ± 0.07	14
0.43	64 ± 3	0.29 ± 0.04	18 ± 10	0.99 ± 0.06	7625 ± 4722	11077 ± 6304	0.68 ± 0.09	12
0.50	60 ± 3	0.26 ± 0.05	14 ± 5	1.00 ± 0.04	7608 ± 3459	10804 ± 5471	0.71 ± 0.08	12
0.58	56 ± 1	0.23 ± 0.02	12 ± 5	1.01 ± 0.05	6828 ± 2792	9294 ± 3345	0.73 ± 0.06	10
0.61	55 ± 4	0.23 ± 0.08	14 ± 7	1.00 ± 0.06	7485 ± 2180	10982 ± 2966	0.69 ± 0.11	12
0.65	50 ± 5	0.29 ± 0.13	13 ± 6	1.00 ± 0.05	8768 ± 3145	11842 ± 4332	0.74 ± 0.08	12
0.69	49 ± 5	0.27 ± 0.11	10 ± 5	0.99 ± 0.04	10990 ± 6261	14443 ± 7412	0.75 ± 0.07	13
Weak inversion-nighttime								
0.14	132 ± 7	0.32 ± 0.05	20 ± 7	0.88 ± 0.08	3676 ± 1346	13525 ± 5833	0.29 ± 0.09	10
0.17	111 ± 6	0.34 ± 0.05	20 ± 8	0.88 ± 0.07	4888 ± 1972	13482 ± 6577	0.38 ± 0.06	9
0.21	97 ± 6	0.35 ± 0.07	21 ± 8	0.88 ± 0.10	5286 ± 2567	12797 ± 5921	0.41 ± 0.11	11
0.32	77 ± 3	0.29 ± 0.04	22 ± 9	0.89 ± 0.10	6647 ± 2950	12589 ± 5010	0.53 ± 0.11	12
0.36	70 ± 7	0.33 ± 0.11	16 ± 6	0.86 ± 0.14	7461 ± 3072	13945 ± 5911	0.55 ± 0.13	13
0.43	65 ± 7	0.28 ± 0.08	19 ± 5	0.90 ± 0.09	8616 ± 3335	15079 ± 6813	0.61 ± 0.16	13
0.50	62 ± 6	0.23 ± 0.08	17 ± 5	0.90 ± 0.07	9896 ± 4043	16176 ± 7583	0.64 ± 0.11	11
0.58	59 ± 7	0.21 ± 0.07	15 ± 7	0.94 ± 0.05	10563 ± 4072	15656 ± 7043	0.70 ± 0.09	14
0.61	57 ± 8	0.22 ± 0.08	19 ± 16	0.95 ± 0.07	9951 ± 3245	14656 ± 6654	0.72 ± 0.11	11
0.65	53 ± 2	0.22 ± 0.03	13 ± 3	0.94 ± 0.06	9475 ± 4018	13231 ± 6221	0.73 ± 0.08	10
0.69	52 ± 4	0.21 ± 0.05	11 ± 3	0.95 ± 0.05	10411 ± 4267	13782 ± 5688	0.76 ± 0.07	10